

Article

Propagation, Scattering and Defect Detection in a Circular Edge with Quasi-Edge Waves

Peifeng Liang ¹, Andrei Kotousov ^{2,*} and Ching Tai Ng ¹

¹ School of Architecture and Civil Engineering, The University of Adelaide, Adelaide, SA 5005, Australia; wayne.liang@adelaide.edu.au (P.L.); alex.ng@adelaide.edu.au (C.T.N.)

² School of Electrical and Mechanical Engineering, The University of Adelaide, Adelaide, SA 5005, Australia

* Correspondence: andrei.kotousov@adelaide.edu.au

Abstract: Structural components with curved edges are common in many engineering designs. Fatigue cracks, corrosion and other types of defects and mechanical damage often initiate from (or are located close to) edges. Damage and defect detection in the presence of complex geometry represents a significant challenge for non-destructive testing (NDT). To address this challenge, this paper investigates the fundamental mode of the quasi-symmetric edge-guided wave (QES_0) propagating along a curved edge, as well as its scattering characteristics in the presence of different types of edge defects. The finite element (FE) approach is used to investigate the propagation and mode shapes of the QES_0 . It was found that the wave attenuation dramatically increases when the radius-to-thickness ratio is less than 20. Moreover, the mode shapes are significantly affected by the waveguide curvature as well as the excitation frequency. Additionally, to evaluate the sensitivity of QES_0 to edge defects, different sizes of edge defects were investigated with the FE model, which validated against experimental results. The validated FE model was further employed to quantify the dependence of the amplitude of scattered waves for different types of edge defects. These studies indicate that the amplitude of scattered wave is very sensitive to the presence of edge defects. The main outcome of this work is the demonstrated ability of the QES_0 wave mode to propagate over long distances and a high sensitivity of this mode to different types of edge defects, which manifest its great potential for detecting and characterising damage near the curved edges of structural components.



Citation: Liang, P.; Kotousov, A.; Ng, C.T. Propagation, Scattering and Defect Detection in a Circular Edge with Quasi-Edge Waves. *Appl. Sci.* **2024**, *14*, 10672. <https://doi.org/10.3390/app142210672>

Academic Editor: Giuseppe Lacidogna

Received: 30 September 2024

Revised: 8 November 2024

Accepted: 16 November 2024

Published: 19 November 2024



Copyright: © 2024 by the authors. Licensee MDPI, Basel, Switzerland. This article is an open access article distributed under the terms and conditions of the Creative Commons Attribution (CC BY) license (<https://creativecommons.org/licenses/by/4.0/>).

Keywords: edge-guided wave; curved structures; defect detection; scattering; non-destructive testing

1. Introduction

Free edges are common features in various engineering components, and these structural features are often subjected to residual stress and are prone to manufacturing defects. As a result, fatigue cracks and other mechanical damage are predominantly initiated and propagate from free edges. Therefore, the defect monitoring of these structural features is of great practical interest.

Ultrasonic-guided waves (UGWs) are considered one of the most effective techniques in non-destructive testing (NDT) and structural health monitoring (SHM). Over the past several decades, the application of UGWs has attracted significant attention to damage and defect detection and monitoring. One main advantage of UGWs is that these waves can propagate in various materials over long distances without significant decay and inspect large areas with a limited number of sensors, which is a prerequisite for SHM systems. In addition, it has been well documented that UGWs can effectively detect various types of damage, such as crack [1–3], corrosion [4–6] and delamination [7–9].

Most studies of UGWs are performed on relatively simple geometries, whereas real structures normally contain many structural features, such as edges, holes, weld seams and other geometric discontinuities, which represent a challenge for defect detection and monitoring. These structure features are normally associated with scattering and

reflection, which induce extra difficulty in the interpretation of the damage signatures. In recent years, several studies indicated that some structural features can also be utilised as a waveguide for NDT or SHM purposes [10–12]. Ultrasonic waves that propagate along those structural features are known as feature-guided waves (FGWs). One main characteristic of FGWs is the concentration of wave energy in the vicinity of the waveguide or structural feature [13–15]. This concentration phenomenon (energy trapping effect) often results in almost lossless signal amplitude, enabling long propagation distance inspection and monitoring, e.g., inaccessible locations. Moreover, it also allows guided waves to inspect specific parts of the structure instead of the entire area to achieve a cost-effective structural integrity inspection [13]. The feasibility of the application of FGWs in damage and defect detection has been widely demonstrated. Fan et al. [14] and Yu et al. [13] investigated the propagation of FGWs along the stiffer, which bonded with an aluminium and composite plate, respectively. Their experimental results demonstrated that the feature-guided shear horizontal wave propagates along a stiffener can be utilised for monitoring the integrity of the bond. Lan et al. [16] theoretically and numerically studied the generation of combined harmonic using an FGW mode propagating in a weld seam. They reported that the generation of a cumulative combined harmonic can be observed in the wave mixing zone, and this phenomenon can be utilised to monitor the progression of material degradation.

Edge-guided waves (EGWs) are a type of FGWs, which are analogous to conventional Rayleigh waves. EGWs propagate along the surface of free edges and are guided by the apex of the plate structure, with a relatively low effective depth of penetration, and hence, they are less affected by the internal features of plate and shell components. In the literature, it has been found that two fundamental wave modes can propagate along these waveguides in an elastic material, namely extensional (ES_0)- and flexural (EA_0)-mode edge-guided waves [17,18]. Wilde et al. [19] proposed a semi-analytical method to obtain the dispersion curve and mode shapes of EGWs propagated in isotropic materials. Hughes et al. [12] conducted an experimental and numerical study on the propagation of ES_0 . They found that the ES_0 is suitable for long-distance inspections in the low range of the frequency to thickness value ($FTV < 5$), while a strong amplitude modulation phenomenon due to the interaction with other wave modes was observed in the high FTV range, $FTV = 2\pi fH / C_T$, where f is the linear frequency, H is the thickness of the waveguide (plate) and C_T is the shear wave speed in the material. In recent publications, the semi-analytical finite element (SAFE) approach has been widely utilised to acquire the propagation characteristics of EGWs in isotropic [20] and anisotropic materials [21]. However, past studies of EGWs were conducted on flat or quasi-flat edge geometries. The effect of the waveguide curvature on the propagation characteristics of EGWs has not been investigated so far. Indeed, analytical approaches or SAFE are currently not available or suitable for the investigation of the characteristics of EGWs that propagate along curved edges due to the complexity of the geometry and associated boundary conditions.

On the other hand, there has been a significant interest in using EGWs for non-destructive damage and defect detection. Chu and Courtney [22] demonstrated the feasibility of ES_0 for the detection of impact damage at the edge of a carbon-fibre-reinforced polymer (CFRP) plate. Zhu et al. [23] studied the effect of sharp and rounded corners on the propagation of ES_0 . They demonstrated that ES_0 can propagate through sharp and rounded corners of plate- and shell-like structures, and that the nonlinear features of the ES_0 wave mode can be used for locating defects and damage. All these features make the ES_0 wave mode very suitable for inspecting inaccessible areas of the structure. Vien et al. [24] investigated the scattering characteristics of ES_0 in the presence of edge cracks located near a racecourse-shaped hole in a flat aluminium plate, which revealed that the amplitude of scattered waves can be utilised for detecting and quantifying edge defects. Despite these promising findings, relatively few studies have focused on damage detection in curved edges. Moreover, the potential of the EGWs in detecting defects along curved edges has not yet been explored despite the fact that these curved edges are often found in many designs, such as in the leading edge of an aircraft's engine inlet.

To improve the understanding of EGWs in detecting damages in curved structural edges, this study aims to investigate the propagation of the fundamental mode of quasi-edge waves (QES_0) along curved edges and explore the scattering characteristics of the QES_0 at notch-like edge defects. In contrast to previous studies on damage or defect detection using EGWs, this study not only focuses on the reflected and transmitted signals but also investigates scattered waves on the curved surface in various directions using the scatter directivity pattern (SDP) approach. Therefore, the outcome of this investigation can also be helpful for the selection and optimisation of sensor configuration for future NDT and SHM systems utilising the QES_0 wave mode.

This paper first presents a 3D FE approach for investigating the effect of waveguide curvature on the propagation characteristics of the QES_0 wave mode in Section 2.1 and is followed by selected simulation results, which are described in Section 2.2. The details of the 3D FE model for investigating the scattering characteristic of QES_0 at different edge defects are presented in Section 2.3. Section 3 is devoted to an experimental study, which is used to validate the developed FE model. The simulation results of the scattering study using the experimentally verified FE model are presented in Section 4. The conclusion and main findings are drawn in Section 5.

2. Numerical Study

In this section, a 3D FE approach for investigating the effect of the waveguide curvature on the propagation characteristic of QES_0 is presented in Section 2.1, followed by the corresponding simulation results in Section 2.2. Section 2.3 details the 3D FE model for investigating the scattering characteristics of the QES_0 wave mode at an edge defect.

2.1. Three-Dimensional FE Model for Investigating Propagation Characteristics of QES_0

The propagation of QES_0 along circular edges was modelled using ABAQUS 2017, and the simulations were performed with the Explicit solver. The configuration of 3D FE models is schematically illustrated in Figure 1. The height and wall thickness were fixed at 200 and 5 mm, respectively. To investigate the effect of curvature on the propagation of QES_0 , FE models were modelled in various radius-to-thickness (R/T) ratios, ranging from 10 to 25 in steps of 5, and from 25 to 100 in steps of 25. It should be noted that the curvature of the edge is inversely proportional to the R/T ratio.

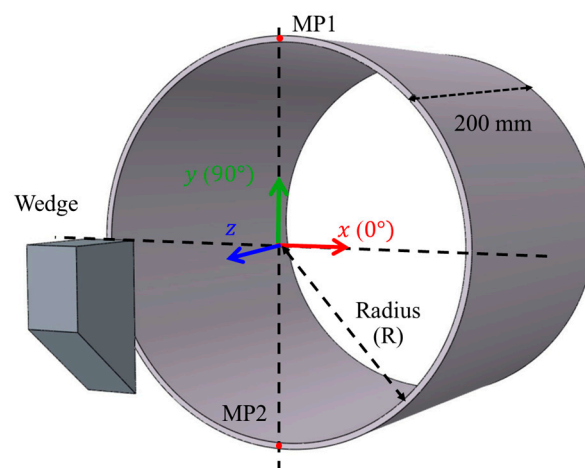


Figure 1. Schematic of the configuration of 3D FE models.

The FE models were meshed with eight-node three-dimensional solid elements with reduced integration (C3D8R), and the meshing technique option was ‘structure’, similar to that in previous studies [20,23]. Due to the non-/minor dispersive nature of EGWs, the wave speeds were very similar in the interested FTV (frequency) range. Hence, the mesh size was selected as 1 mm^3 . This mesh size ensures that at least 15 elements exist

per wavelength for the highest frequency of interest (300 kHz or $FTV = 3$). The time steps of simulations were automatically determined by the Explicit solver, which employed the central difference method. To maximise the transfer of input energy to the QES_0 mode while minimising the influence of other generated wave modes, wedge excitation was used. The angle of the wedge was determined by Snell's law, as follows: $\theta_{\text{wedge}} = \sin^{-1}(C_{L(\text{wedge})}/C_{EW})$, where θ_{wedge} is the wedge angle, $C_{L(\text{wedge})}$ is the longitudinal wave speed of the wedge material and C_{EW} is the wave speed of the excited EGW mode. In this study, the longitudinal wave speed of the wedge is around 2300 m/s, and the wave speed of ES_0 is about 2870 m/s. Hence, the wedge angle is determined as 53° . The interaction between the wedge and specimen was defined as a surface-based 'Tie' constraint to enable the transmission of input energy to the specimen. The incident wave in the wedge was generated by applying a pressure of 10 MPa perpendicular to the circular excitation area, which is located on the wedge slope. The excitation area has a diameter of 22 mm (the same size as the actual transducer used in the experimental study). The excitation signals are Hanning-window-modulated eight-cycle sinusoidal tone bursts. The material properties of different components of the models are listed in Table 1.

Table 1. Material properties of the FE model.

Part	Material	Density (kg/m ³)	Elastic Modulus (GPa)	Poisson's Ratio	α Damping
Specimen	Aluminium	2704.00	70.00	0.30	N/A
Wedge	Polystone	351.40	0.90	0.40	28,783.30

Figure 2a,b show the wedge excitation and the propagation of QES_0 in a curved edge, respectively. Most of the input energy was concentrated and propagated along the curved edge in the clockwise direction. Meanwhile, a backward EGW, which has a much smaller magnitude, was generated and propagated along the anticlockwise direction.

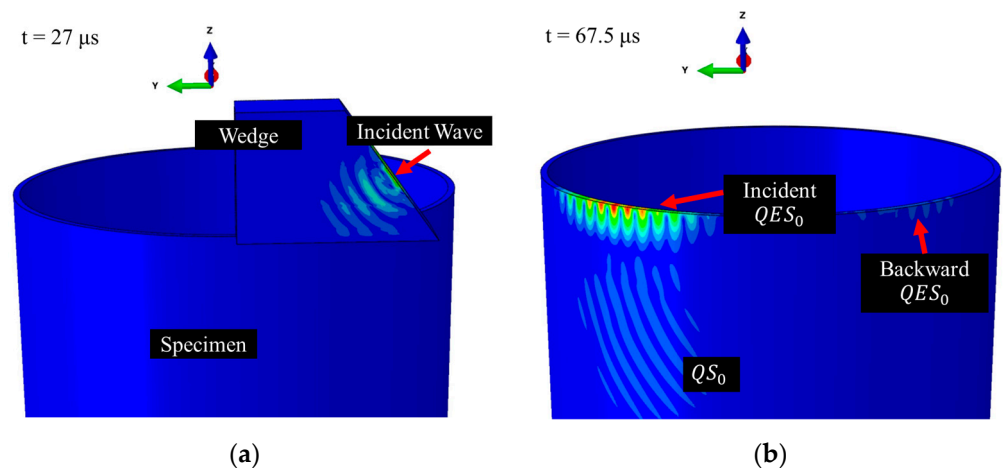


Figure 2. Snapshot of the 3D FE model's ($R/T = 20$) simulation results of (a) the wedge excitation and (b) propagation of QES_0 .

Since wave motion can be largely affected by the geometric of the propagation medium, it is necessary to separate the QES_0 wave mode from other guided and bulk wave modes. To identify the wave mode of generated and measured signals, a frequency–wavenumber analysis was conducted using a two-dimensional fast Fourier transform (2D FFT). The simulation results obtained from the FE model with an R/T ratio of 10, which is the smallest R/T ratio of interest, were investigated. The normal displacement of the top edge (U_z) was extracted from 35 continuous nodes (starting from measurement point 1) along the wave propagation direction, with intervals of around 1 mm.

The same modelling procedure outlined in Section 2.1 was also applied to another 3D FE plate model ($R/T = \infty$), which simulates the propagation of ES_0 in a 5 mm thick flat plate with the same material properties, for comparison purposes. The simulation results from this FE model can be considered as a benchmark as they are not affected by the effect of the curvature (straight edge). This particular 3D model has been analytically and experimentally well validated in previous work [12]. It should be noted that the distance between measurement points and the wedge in this model is approximately the same as the corresponding curved edge model. The excitation frequency is 200 kHz, which has a corresponding FTV of 2. Then, the 2D FFT results were compared with the dispersion curve of ES_0 propagates in an ideal waveguide with the same thickness [20].

Figure 3a,b show the 2D FFT results for the propagation of ES_0 in a flat plate and QES_0 in a curved edge, respectively. The results indicate that the only propagating wave mode at 200 kHz in curved edge is QES_0 , which is very similar to the propagation of the ES_0 wave mode in terms of wavenumber.

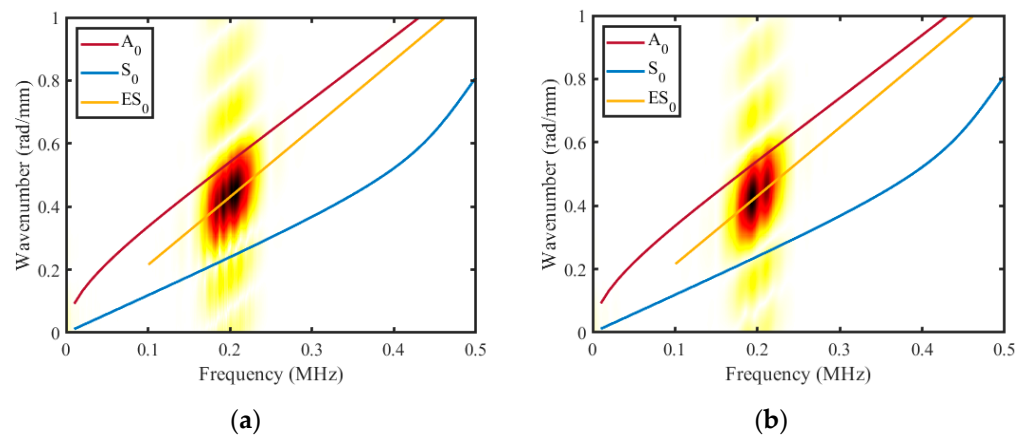


Figure 3. A 2D FFT plot for FE results of (a) plate and (b) $R/T = 10$ curved edge model.

2.2. Effect of the Curvature on the Propagation Characteristics of QES_0

2.2.1. Attenuation

In this section, the effect of the radius of curvature on the attenuation of the QES_0 wave mode is discussed. To quantify the attenuation of QES_0 for different curvatures, a coefficient of attenuation (μ) was introduced and defined as follows:

$$\mu = \frac{A_{MP1} - A_{MP2}}{d} \quad (1)$$

where A_{MP1} and A_{MP2} are the amplitudes of measurement points (MP) 1 and 2, respectively, and d is the propagation distance that is half the perimeter of the corresponding model. It should be noted that the amplitudes were normalised by the corresponding A_{MP1} in the calculation of μ .

Figure 4 presents the relationship between μ and the R/T ratio. It can be observed that the value of μ increases with the FTV in the case of the same R/T ratio. On the other hand, it can also be observed that the value of μ is highly correlative to the R/T ratio. At the stage of the R/T ratio ranging from 100 to 20, the value of μ is similar, while the value of μ dramatically increases when the R/T ratio changes from 20 to 10. This phenomenon aligns with the corresponding 2D FFT results shown in Figure 3a,b, which indicate a lower energy concentration within the bandwidth of excitation frequency as the R/T ratio of the waveguide decreases.

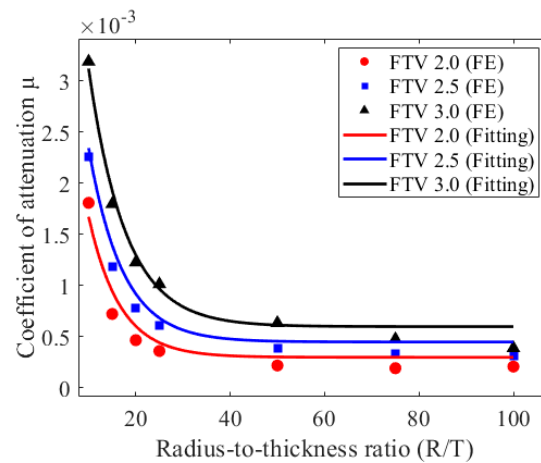


Figure 4. Coefficient of attenuation against R/T ratio.

To better describe the correlation between μ and the R/T ratio across various *FTVs*, a curve-fitting analysis was conducted using the FE simulation results. The establishment of algebraic expression for fitting can help to predict the effect of waveguide curvature on the propagation of QES_0 . The procedure for establishing this algebraic expression of the curve-fitting analysis is as follows:

- By observing the relationship between μ and R/T ratio in Figure 4, it was found that the function of $y = A \cdot e^{(-Bx)} + C$ has a good correlation to the simulated data, where A , B and C are parameters related to *FTV*, and x is the ratio of R/T.
- The nonlinear least-squares optimisation was employed to find the values of A , B and C parameters using an iteration procedure, which minimises the residual sum of squares (RSSs) between predicted values and the corresponding FE simulation results.
- To generalise the fitting between μ and R/T ratio across different *FTVs*, the parameters of A , B and C in different *FTV* cases were presented as linear.

Finally, the relationship between μ and the R/T ratio for different *FTVs* can be expressed as

$$\mu = Ae^{-B \cdot \frac{R}{T}} + C \quad (2)$$

where $A = 0.0029FTV + 0.0004$, $B = -0.0224FTV - 0.1955$ and $C = 0.0003FTV - 0.003$, respectively. Figure 4 also shows a comparison between the FE simulation results and the predicted value (solid line) using Equation (2). It can be observed that there is a good agreement between Equation (2) and the simulation results.

2.2.2. Mode Shapes

To investigate the effect of the curvature of a waveguide on mode shapes of the QES_0 wave mode, the normal displacement of nodes along lines 1 (U_z) and 2 (U_y) was extracted (see Figure 5). Figure 5a,b illustrate the location of lines 1 and 2, respectively, where line 1 is located on the top of the surface of the edge and line 2 is on the outer surface of the specimen. The simulation results from the present models were compared with the corresponding simulation results for ES_0 , which were validated with analytical results [12].

Figure 6a–c show the normal displacement (U_z) of the top edge extracted from line 1. The data were normalised with the corresponding maximum value. The mode shape of ES_0 (marked by the green line) can be seen to be the baseline. It can be observed that the mode shape of ES_0 was symmetric about the mid-plane of the top edge surface, and that the amplitudes increased from the mid-plane toward both the outer and inner sides. Meanwhile, it can also be observed that the symmetricity of the QES_0 was largely affected by the waveguide curvature. With the decrease in the R/T ratio, the difference in amplitudes between the outer and inner sides of the curved edge increased. In addition, it

can also be noted that the mode shape of QES_0 was more affected by the change in the R/T ratio in the case of high frequencies.

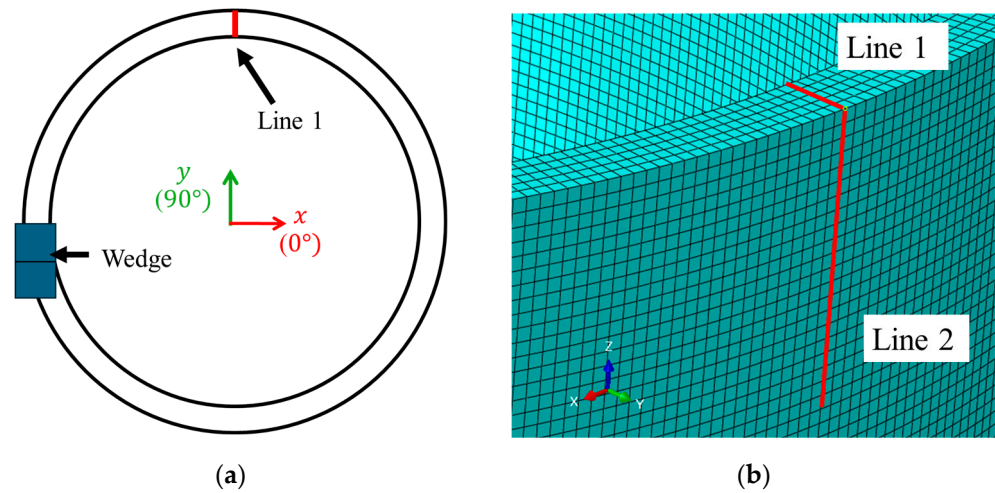


Figure 5. Schematic of the location of measurement points for extracting mode shapes: (a) top view and (b) zoom-in view.

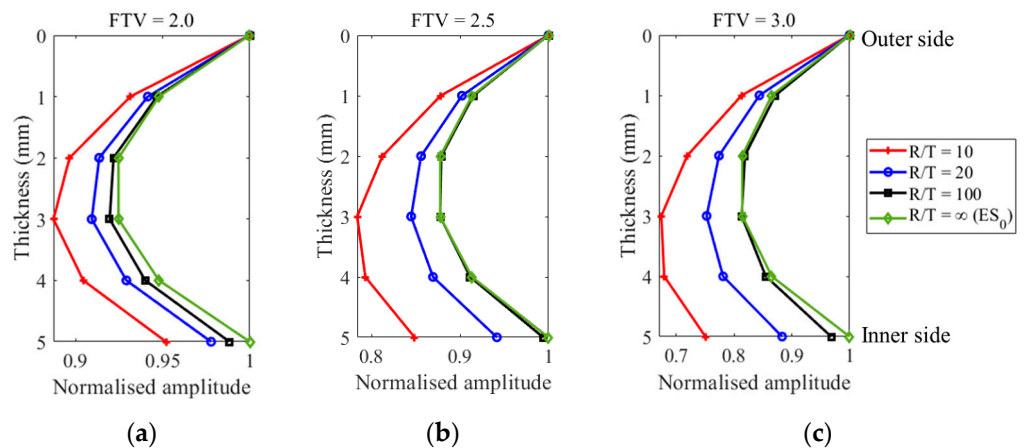


Figure 6. Normal displacement (U_z) of line 1 with different R/T ratios: (a) FTV = 2.0, (b) 2.5, and (c) 3.0.

Figure 7a–c show the normal displacements (U_y) of the side surface, which are extracted from line 2. It can be observed that the amplitudes of ES_0 and QES_0 waves rapidly decayed with the depth from the top edge surface. With the increase in excitation frequency, the effective depths of ES_0 and QES_0 were closer to the surface of the top edge. This behaviour is similar to the classical Rayleigh wave mode, where energy is more concentrated on the surface with the increase in the excitation frequency [25]. In addition, it can also be observed that the amplitudes of leaky waves from QES_0 is highly correlated to the waveguide curvature. With the decrease in the R/T ratio (larger curvature), more energy was transferred from QES_0 to leaky waves that propagated on the side surfaces of the edge.

The results from this numerical case study of QES_0 , propagated along curved edges, provide potential guidelines for optimising sensor numbers and locations to maximise the signal-to-noise ratio. From a practical application perspective, when inspecting a relatively thick curved edge of a structural component, a higher wave magnitude can be measured from a location on the top edge surface that is close to the outer side, compared to the inner surface or mid-plane (see Figure 6a–c).

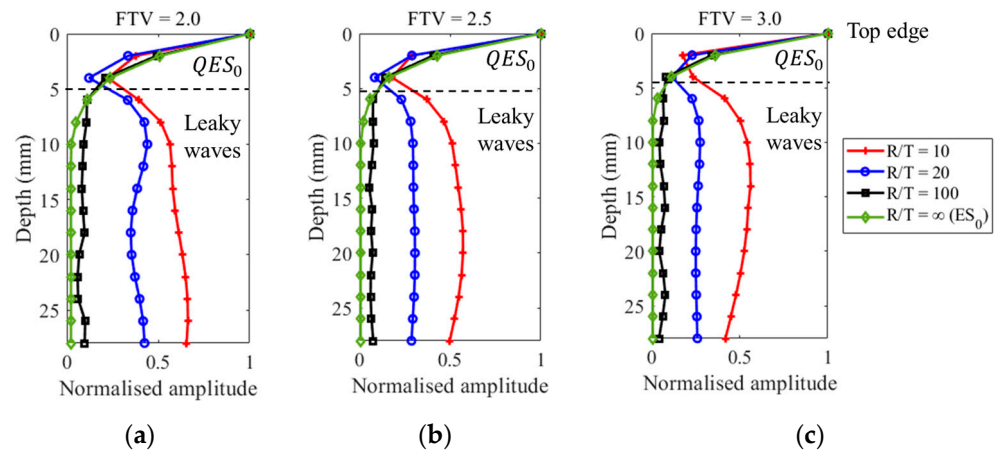


Figure 7. Normal displacement (U_2) of line 2 at FTV = (a) 2.0, (b) 2.5 and (c) 3.0.

2.3. A 3D FE Model for Investigating Scattering Characteristics of the QES_0 Wave Mode at an Edge Defect

In this section, the R/T ratio of the 3D FE model is fixed at 20. The modelling approach is largely the same as that which was described in Section 2.1. To investigate the scattering characteristic of QES_0 at edge defects, a narrow notch-like edge defect was modelled by removing elements from the model as shown in Figure 8. The location of the edge defect is in 45° direction, as illustrated in Figure 8a. The edge defect was modelled as 1 mm thick (along the wave propagation direction), which avoids the possible contact between the surfaces of the edge defect. To investigate the dependence of amplitudes of scattered waves and the size of the edge defect, the depth of the through-thickness edge defect was modelled, ranging from 2 to 14 mm with increments of 3 mm. Figure 8b presents a snapshot of an 8 mm long through-thickness edge defect in the FE model. To study the scattering characteristics of QES_0 at partially through-thickness edge defects, two types of partially through-thickness edge defects with a depth of 8 mm were investigated with the developed FE model. Types I and II of partially through-thickness edge defects were located in the inner- and outer-side surfaces of the edge, respectively, as illustrated in Figure 8c,d. The width of the partially through-thickness edge ranged from 1 to 4 mm with increments of 1 mm.

The reflected and transmitted waves were obtained from MP1 and MP2, respectively, whose locations are also illustrated in Figure 8a. In addition, to investigate the amplitude of scattered waves in different directions, nine measurement points, centred at the base of the edge defect, were assigned on the side surface of the edge ranging from 0 to -180° in steps of -22.5° , as shown in Figure 9a,b. It should be noted that the distance between these measurement points and the base of the edge defects was fixed at 50 mm. To allow for a direct comparison between the amplitudes of scattered waves collected in different measurement points, the U_x displacement of each measurement point was converted to the corresponding normal displacement (u_{normal}) of the side surface, as illustrated in Figure 9c.

Figure 10a–c and Figure 10d–f present the typical contour plots of FE simulation results for QES_0 before and after encountering through-thickness edge defects with depths of 2, 8, and 14 mm, respectively. The central frequency of the input signal was 200 kHz. Figure 10d–f illustrate that the magnitudes of scattered waves are highly correlated to the depth of the edge defect, which also reveals the mode conversion between QES_0 and scattered waves.

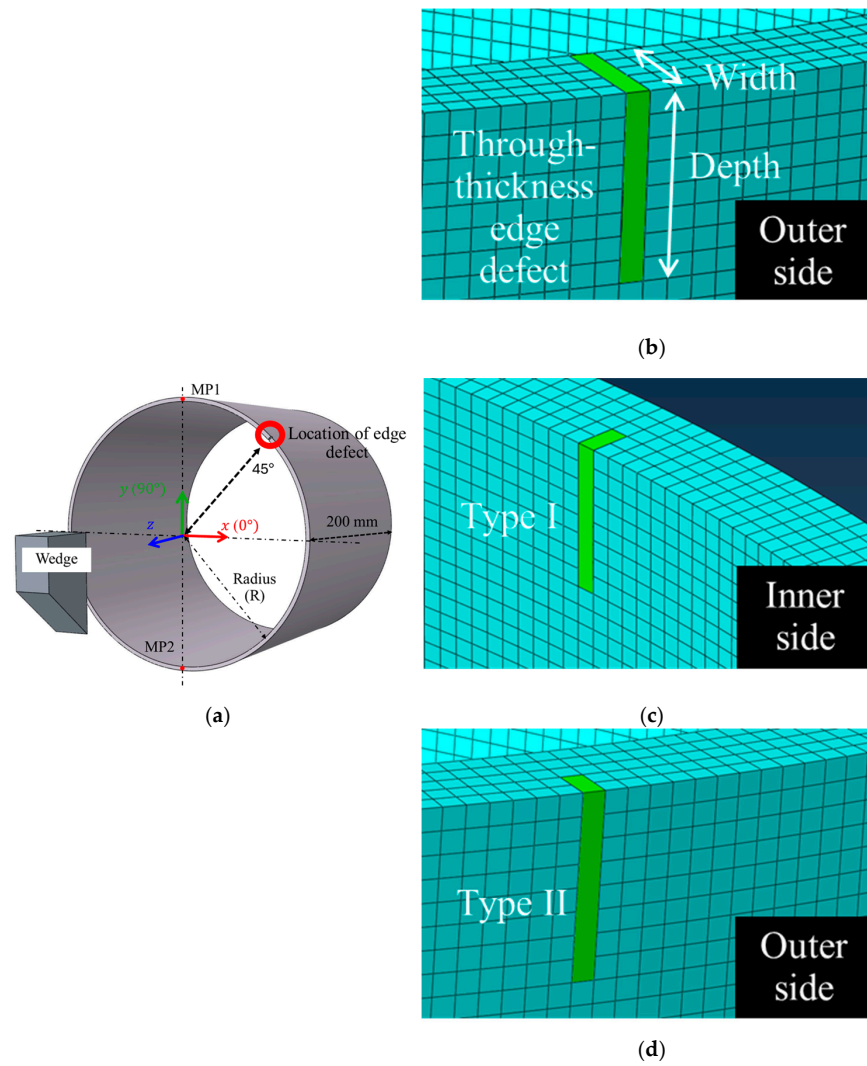


Figure 8. (a) Schematic of edge defect location in the 3D FE model. Snapshot of (b) through-thickness (c) type I and (d) type II of partially through-thickness edge defect.

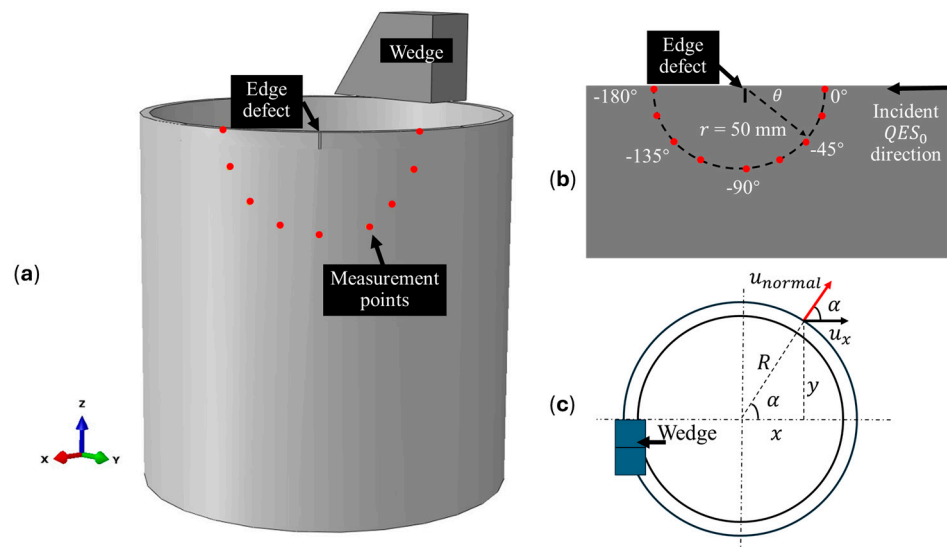


Figure 9. (a) Schematic of the location of measurement points for measuring scattered waves. (b) Configuration details of measurement points for measuring scattered waves. (c) Schematic diagram of conversion between u_x and u_{normal} of the measurement point for the scattering study.

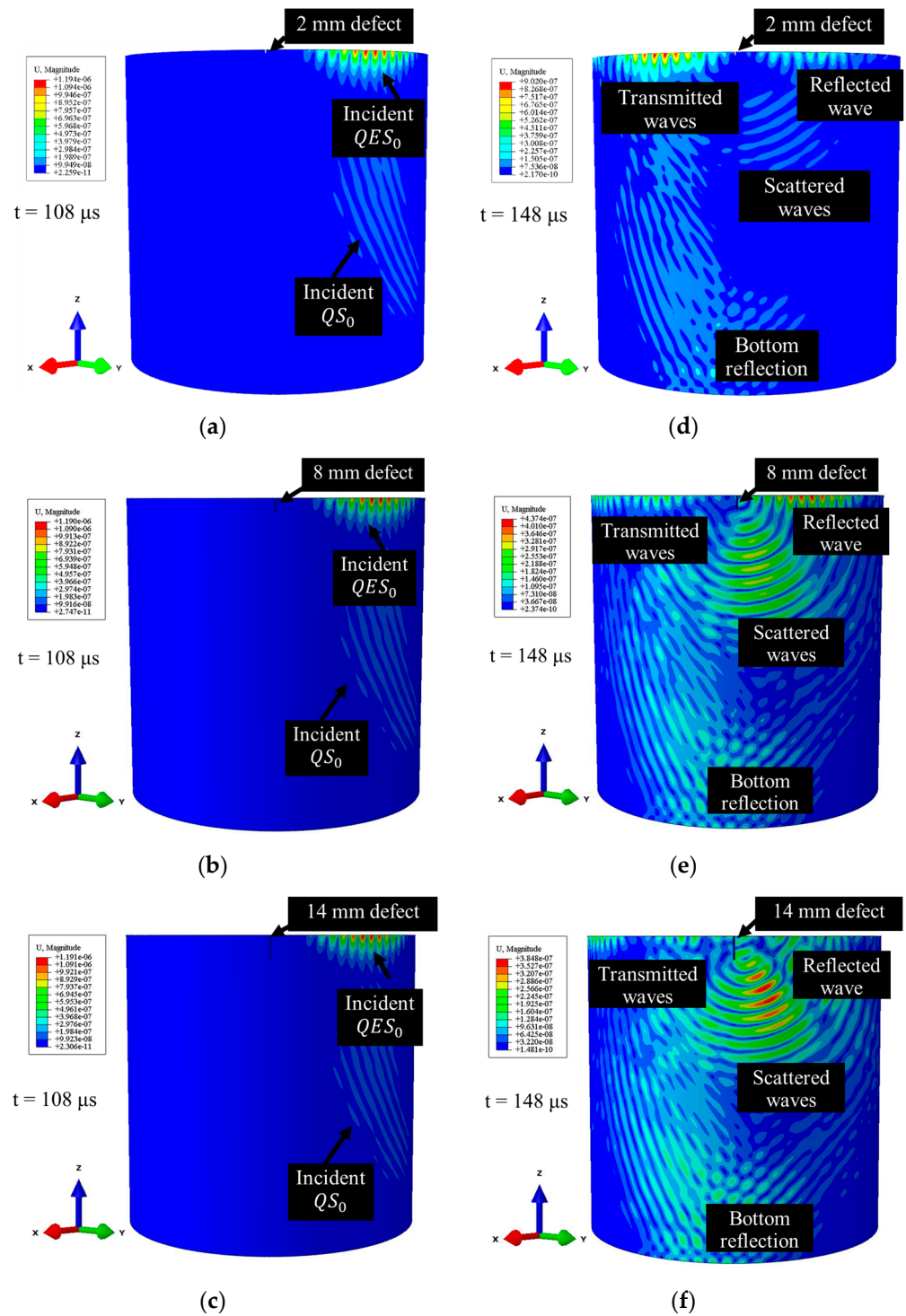


Figure 10. Snapshot of QES_0 (FTV = 2) propagation (a–c) before and (d–f) after encountering the through-thickness edge defect with depths of 2 (a,d), 8 (b,e) and 14 (c,f) mm.

3. Experimental Study

This section presents an experimental study for the verification of the 3D FE approach described in Section 2.3. The specimen details and experimental setup for generating and sensing the QES_0 wave mode is presented in Sections 3.1 and 3.2, respectively. Finally, in Section 3.3, a comparison between the experimentally measured and the corresponding FE simulation results is presented.

3.1. Specimen

The tested specimen was an aluminium tube that had an outer diameter of 200 mm, a wall thickness of 5 mm, and a height of 200 mm. These were the same dimensions as those of the FE model described in Section 2.3. A 1 mm thick through-thickness edge defect was manually created on the top edge of the specimen in a 45° direction. During the experiment, the depth of the through-thickness edge defect was increased from 2 to 14 mm with intervals of 3 mm.

3.2. Experimental Setup

The experimental setup for generating and sensing QES_0 is presented in Figure 11a. The input signal, an eight-cycle Hann-windowed tone burst, was generated using a signal generator (National Instrument PXIe-5412). The central frequency of the input signal was 200 kHz. Then, a signal amplifier (Ciprian HVA-800-A) was used to amplify the input signal to ± 200 V. The amplified signal was then sent to a transducer (ULTRAN-GC200), which could generate a longitudinal wave. The transducer was installed on a 53° wedge, which was made of 'Polystone', as shown in Figure 11b. The wedge was clamped to the top edge of an aluminium tube-like specimen. A coupling gel (Dow corning high-vacuum grease) was applied on the interface between the wedge and the top edge of the specimen to ensure the effective transmission of the longitudinal wave from the wedge into the specimen, thereby generating the QES_0 mode. The locations of the two measurement points for measuring reflected and transmitted waves were defined as consistent with the configuration of the FE model described in Section 2.3. The normal displacement of the measurement points located on the top edge was collected by a one-dimensional (1D) laser Doppler vibrometer (Polytech PSV-400-M2-20). The measurement distance was fixed at 1 m. The sampling frequency was set to 25.6 MHz, and each measurement was averaged by 200 acquisitions. To improve the signal-to-noise ratio, the edge was coated with reflective paint, and a low-pass filter with a cut-off frequency of 1 MHz was applied to the laser Doppler vibrometer.

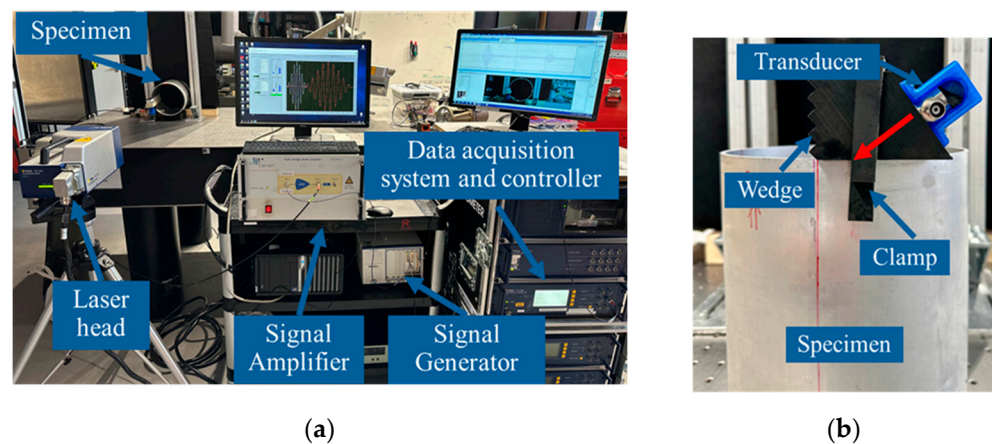


Figure 11. (a) Experimental setup. (b) Configuration of wedge excitation.

3.3. Reflection and Transmission at Edge Defects

In this section, the experimental results were compared with the corresponding FE simulation results for validation purposes. The reflected and transmitted waves were collected at MP1 and 2, respectively, which was the same as the FE configuration shown in Section 2.3.

Figure 12a shows a comparison between numerical and experimental time domain signals in intact conditions, while Figure 12b compares the FE and experimental time domain signals in the presence of a 2 mm deep edge defect. Both experimental and numerical data were normalised by the corresponding maximum absolute amplitude in the time domain. The arrival time of the incident wave and reflected wave was precisely predicted

by the FE simulation, as shown in Figure 12b. The minor phase shift in the incident and reflected wave can be attributed to the slight misalignment of the wedge in the experiment.

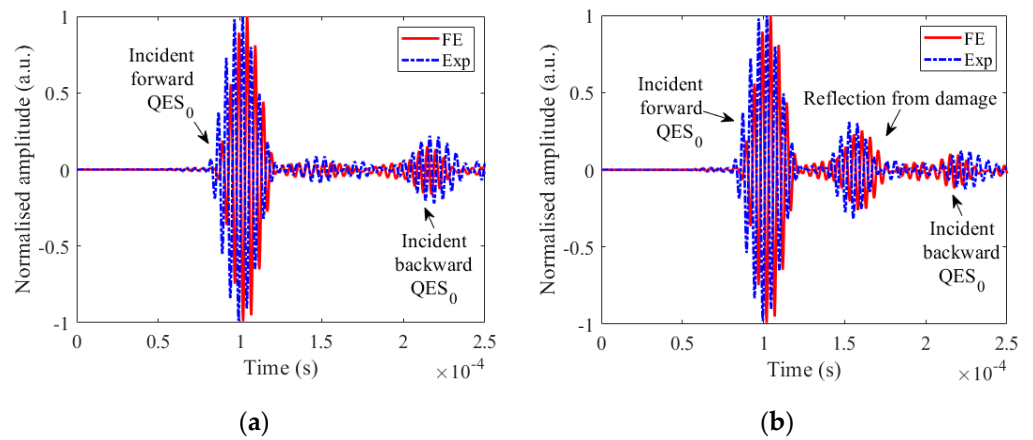


Figure 12. Comparison between numerical and experimental time domain data of MP1 in (a) intact and (b) presence of a 2 mm deep through-thickness edge defect.

Figure 13a,b present the ratio of amplitudes of reflected (A_r) and transmitted (A_t) waves from the edge defect to the amplitude of the incident wave (A_i), respectively. The amplitudes of reflected and transmitted waves were normalised by the amplitude incident wave at MP1. The reflection (R_r)-and-transmission (R_t) ratio was defined as $R_r = A_r/A_i$ and $R_t = A_t/A_i$, respectively. It can be observed that the 3D FE model well predicted the trend of reflection-and-transmission ratio with the change in defect depth-to-wavelength ratio. The discrepancy can be attributed to the misalignment of the laser beam. In the experiment, it is not pragmatic to ensure that the laser beam is perfectly perpendicular to the mid-plane of the edge due to the thin edge thickness of the specimen, which consequently causes differences between amplitudes of experimentally measured signal and corresponding numerical data; the reason for this phenomenon is discussed in Section 2.2.2. Overall, there is good agreement between FE simulated results and the experimental data, which means that the developed 3D FE approach is adequate and capable of investigating the interaction between the incident QES_0 wave mode and the narrow edge defect in the curved edge.

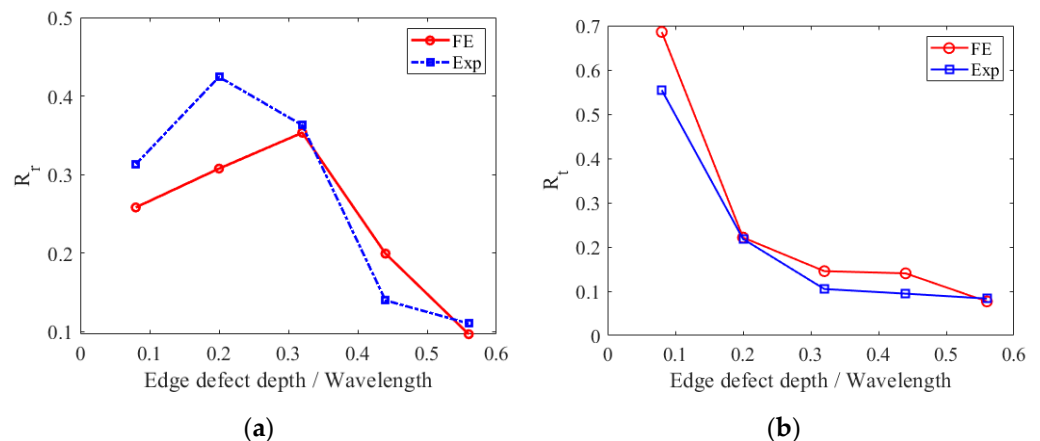


Figure 13. Ratio of (a) reflection and (b) transmission against the ratio of defect depth to wavelength.

4. Directivity Pattern of Scattered Waves

In this section, the experimental validated FE model was employed to investigate the scattering characteristics of QES_0 at a defect in the curved edge. The configuration of measurement points for calculating the scattering directivity pattern (SDP) is presented

in Figure 9. To isolate scattered waves from the incident wave, the baseline subtraction method was employed. The normal displacement of scattered waves U_S is defined as

$$U_S = U_D - U_I \quad (3)$$

where U_I and U_D are the normal displacements of the measurement point in intact and damaged conditions, respectively. It should be noted that all SDPs in this study are normalised by the maximum absolute amplitude of the incident wave at the measurement point of 0° direction.

4.1. Influence of the Size of Through-Thickness Edge Defect

The SDPs of defect depths at 2, 8 and 14 mm were investigated. The corresponding defect depth-to-wavelength ratios were 0.08, 0.32 and 0.56, respectively. Figure 14a–c present the SDPs of edge defects with depths of 2, 8 and 14 mm, respectively. The results indicate that the maximum amplitude of scattered waves increased with the defect size. The energy of scattered waves was mainly located in the forward direction as well as directions that were perpendicular to the wave propagation direction, while the energy of backward scattered waves in the 0° direction was relatively weak. Meanwhile, the forward components of scattered waves have a relatively larger amplitude. It can also be observed that the amplitudes of backward scattered waves in the direction of -67.5° significantly increased with the defect depth-to-wavelength ratio.

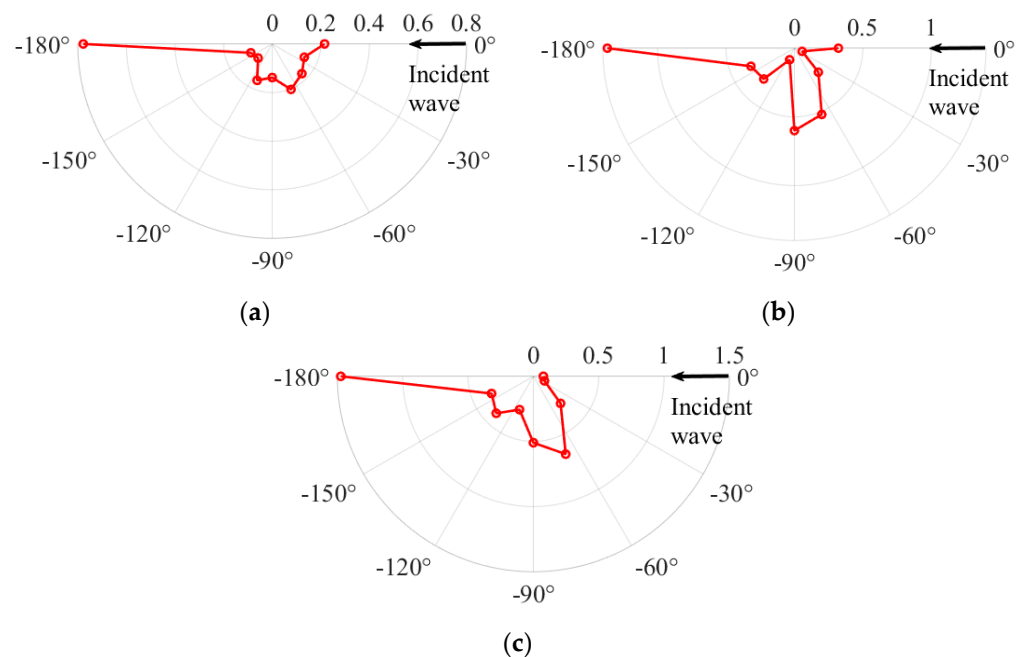


Figure 14. Polar plot of normalised maximum amplitudes of scattered waves at the through-thickness edge defects with depths of (a) 2, (b) 8 and (c) 14 mm.

4.2. Influence of Location and Size of Partially Through-Thickness Edge Defect

Figure 15a–d show the comparison between the 8 mm deep (defect depth-to-wavelength ratios = 0.32) types I (located on the inner side) and II (located on the outer side) of partially through-thickness edge defects with widths of 1, 2, 3 and 4 mm, respectively. All the SDPs in Figure 15 show that the energy of scattered waves are concentrated in forward and normal directions relative to the incident wave propagation direction, which is similar to the case of the through-thickness edge defect. In Figure 15, the SDPs of type I are similar to the SDPs of type II in the corresponding dimension. Compared to type I, the amplitudes of scattered waves of type II in the -135° direction are relatively stronger.

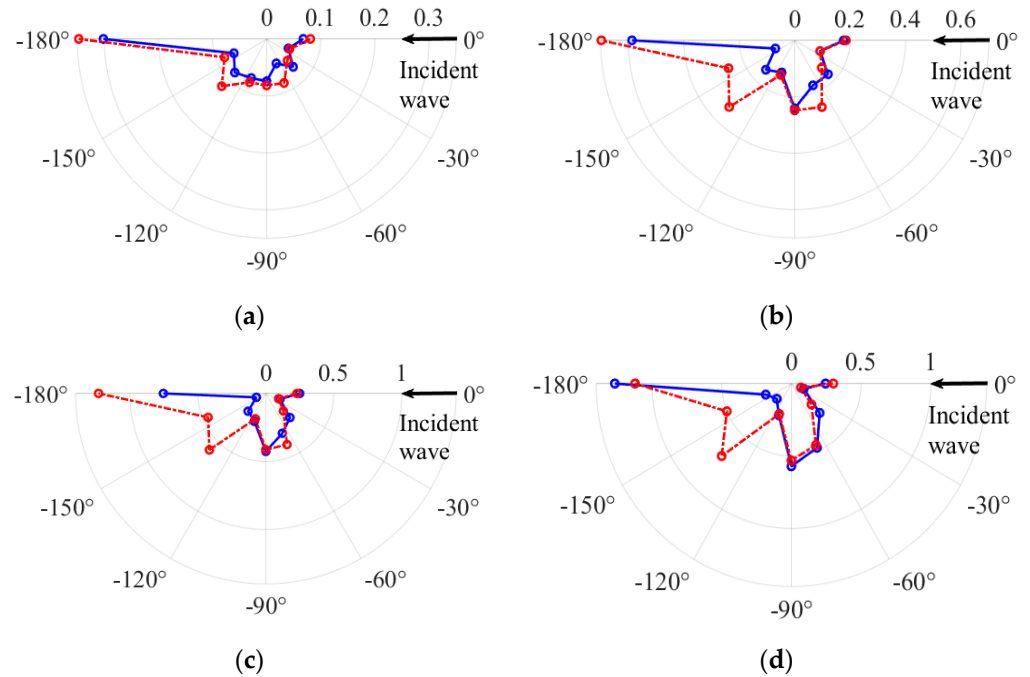


Figure 15. Polar plot of the normalised maximum amplitudes of scattered waves of type I (blue solid line) and type II (red dashed line) edge defects with widths of (a) 1, (b) 2, (c) 3 and (d) 4 mm.

Figure 16a,b present the comparison of SDPs for the edge defects of types I and II with different widths, respectively. The black solid line can be taken as a benchmark, which represents the scattered waves for an 8 mm deep through-thickness edge defect. It can be observed that the amplitude of scattered waves increased with the width of defects. The energy of scattered waves at the type I edge defect is concentrated in the forward and normal directions relative to the incident wave propagation direction. For type II, the energy of scattered waves not only increased in forward and normal directions but also in the -135° direction, as shown in Figure 16b. However, the amplitudes of scattered waves significantly decreased at the dimension of 5 mm, where type II converts to a through-thickness edge defect.

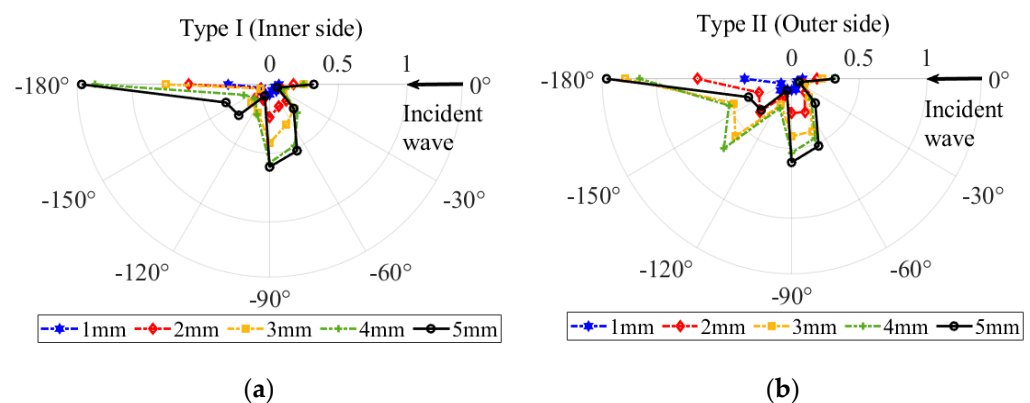


Figure 16. Polar plot of the normalised maximum amplitudes of scattered waves of (a) type I (located on the inner side) and (b) type II (located on the outer side) partially through-thickness edge defects with various widths.

To further elucidate the correlation between defect width and the amplitudes of scattered waves, Figure 17 presents the dependences of the amplitudes of scattered waves in various directions as a function of the defect width.

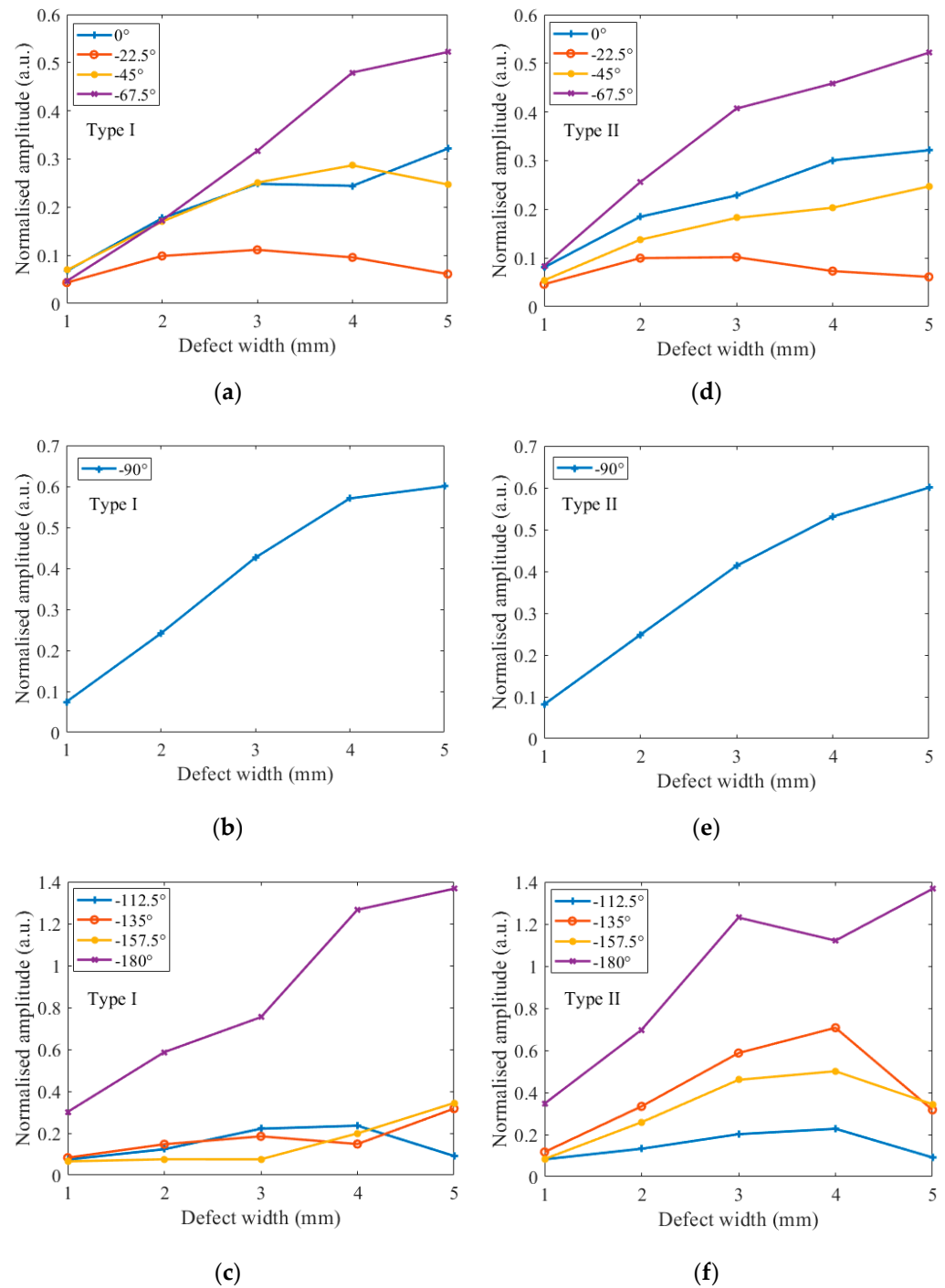


Figure 17. Normalised amplitudes of scattered waves of type I (located on the inner side) in (a) forward, (b) normal and (c) backward direction; normalised amplitudes of scattered waves of type II (located on the inner side) partially through-thickness edge defect in (d) forward, (e) normal, and (f) backward direction.

Figure 17a–c show the normalised amplitudes of forward, normal and backward scattered waves at the type I edge defect (see Figure 8c) with various widths. Figure 17a shows the normalised amplitudes of forward scattered waves in the directions of -180° , -157.5° , -135° and -112.5° (with respect to the incident wave direction), respectively. It can be observed that the amplitudes of scattered waves in the directions of -180° , -157.5° and -135° show an increasing trend with the defect width, while the change in amplitudes of scattered waves in the direction of -180° are relatively stronger than

the other two directions. For forward scattered waves in the direction of -112.5° , the amplitude increases with the defect width in the range from 1 to 4 mm. However, when the defect geometry approaches a through-thickness geometry, the amplitude of scattered waves in the direction of -112.5° decreases.

Figure 17b shows the scattered wave amplitude in the normal direction (-90°) relative to the incident wave propagation direction. The results indicate that the amplitude of scattered waves increases proportionally with the width of the type I edge defect in the range between 1 and 4 mm. However, the slope becomes less steep when the width increases from 4 to 5 mm.

Figure 17c shows the backward-scattered-wave amplitudes in the directions of -67.5° , -45° , -22.5° and 0° . For the backward scattered waves in the direction of -67.5° , the scattered wave amplitudes rise with the defect width and exhibit a similar trend as normal scattered waves (as shown in Figure 17b), while magnitudes are relatively smaller than those in the normal direction. For backward scattered waves in the directions of -45° and -22.5° , the wave amplitudes grow when the defect width increases from 1 to 4 mm and decreases when the defect shape approaches through-the-thickness geometry. In the incident wave direction (0°), the amplitudes of backward scattered waves mainly increase with the defect size, but the dependence is quite weak for a defect width between 3 and 4 mm. Additionally, other than -180° direction, the magnitude of backward scattered waves is relatively greater than for forward scattered waves, which is shown in Figure 17a.

Figure 17d–f present the normalised amplitudes of forward, normal and backward scattered waves at the type II edge defect, with various widths (see Figure 8d). Figure 17d shows the normalised amplitudes of forward scattered waves in the directions of -180° , -157.5° , -135° and -112.5° , respectively. It can be observed from Figure 17a that forward scattered waves in the direction of -180° significantly increase with the defect width. Meanwhile, the forward scattered waves in the other directions show a similar trend as for type I edge defects.

Figure 17e presents the normal scattered waves (-90°). The overall responses are identical to the corresponding results of the type I edge defect (see Figure 17b), while the change in scattering amplitude is relatively larger when the width of the edge defect increases from 4 to 5 mm.

Figure 17f shows the backward scattering amplitudes in -67.5° , -45° , -22.5° and 0° directions. It can be observed that the backward scattered waves in the direction of -67.5° are relatively stronger than the other three different propagation angles, which is similar to the corresponding tendency shown in Figure 17c. The aforementioned results and analysis indicate that forward, normal and oblique backward directions are all suitable for detection and characterising internal, outer and through-the-thickness edge defects.

5. Conclusions

An investigation of the propagation and scattering characteristics of the QES_0 wave mode in circular edges of structural components was presented in this paper. In the first part of this article, the effect of waveguide curvature on the attenuation and mode shapes of QES_0 was investigated using the FE approach. The FE models were constructed for a wide range of R/T ratios, ranging from 10 to 100, covering most curvatures in practical applications. The FE simulation results indicated that the coefficient of attenuation exponentially increased with the waveguide curvature. In addition, from the analysis of the mode shapes, it was found that the normal displacement of QES_0 at the top edge, close to the outer-side surface, was larger than that of the corresponding location close to the inner-side surface. This characteristic can be used for improving signal-to-noise ratio in practical applications of the QES_0 wave mode, specifically for relatively thick components.

In the second part of this study, the reflection-and-transmission ratio of QES_0 at edge defects was first experimentally and numerically investigated. The outcomes indicated that the 3D FE approach is capable of accurately predicting the interaction between the QES_0 wave mode and different dimension's edge defects. The experimentally validated

3D FE model was further employed to explore the scattering characteristics of the QES_0 wave mode for various geometries of edge defects, representing possible edge defects. The results indicated that the scattered waves have relatively large amplitudes in both forward and perpendicular directions with respect to the incident wave propagation direction. Meanwhile, compared to the type I (inner side) partially through-thickness edge defect, the QES_0 at the type II (outer side) edge defect has a relatively strong scattered wave component between the forward and normal directions of incident wave direction.

Although the results are promising, underlying assumptions of the developed FE model should be considered when comparing experimental results with numerical simulations. The effect of material damping was not modelled; therefore, only the effect of waveguide curvature on the attenuation of QES_0 was revealed in the FE simulations. To fully understand the propagation characteristics of QES_0 , future studies can incorporate the effect of material damping on the propagation of the QES_0 wave mode. Moreover, it is assumed in the FE model that the surfaces of the specimen are perfectly smooth, which is not the case for real structural components. Since EGWs are surface waves, the roughness of surfaces could significantly affect the propagation of the QES_0 wave mode, specifically when the wavelength becomes comparable with the characteristic size of the asperities or other structural imperfections. In addition, the contact condition between the interfaces of the wedge and specimen in the FE model is defined as a ‘Tie’ constraint, which may differ from the conditions in actual measurements.

In summary, this study provided fundamental insights into the propagation of QES_0 in a curved waveguide, and the scattering characteristics of QES_0 at various shapes of edge defects. The main practical outcome of this work is the demonstration of the high sensitivity of the QES_0 wave mode to different types of edge defects and its ability to propagate over long distances (at high R/T ratios, i.e., above 20). This capability can be utilised for inspecting defects in inaccessible areas of structures. Overall, the outcomes highlight the significant potential of this guided wave mode for future NDT and SHM systems in detecting and characterising damage along the curved edges of structural components.

Author Contributions: Conceptualisation, P.L. and A.K.; software, P.L.; validation, P.L., A.K. and C.T.N.; investigation, P.L.; resources, A.K. and C.T.N.; writing—original draft preparation, P.L.; writing—review and editing, A.K. and C.T.N.; supervision, C.T.N. and A.K.; funding acquisition, A.K. and C.T.N. All authors have read and agreed to the published version of the manuscript.

Funding: This study was funded by the Australia Research Council (ARC) under grant numbers DP200102300 and DP210103307. The authors would like to express deep appreciation for this support.

Institutional Review Board Statement: Not applicable.

Informed Consent Statement: Not applicable.

Data Availability Statement: The raw data supporting the conclusions of this article will be made available by the authors on request.

Conflicts of Interest: The authors declare no conflicts of interest.

References

1. Masserey, B.; Mazza, E. Ultrasonic sizing of short surface cracks. *Ultrasonics* **2007**, *46*, 195–204. [[CrossRef](#)] [[PubMed](#)]
2. Guan, R.; Lu, Y.; Wang, K.; Su, Z. Fatigue crack detection in pipes with multiple mode nonlinear guided waves. *Struct. Health Monit.* **2018**, *18*, 180–192. [[CrossRef](#)]
3. Zhu, W.; Xu, Z.; Xiang, Y.; Liu, C.; Deng, M.; Qiu, X.; Sun, D.; Xuan, F. Nonlinear ultrasonic detection of partially closed cracks in metal plates using static component of lamb waves. *NDT E Int.* **2021**, *124*, 102538. [[CrossRef](#)]
4. Zima, B.; Woloszyk, K.; Garbatov, Y. Experimental and numerical identification of corrosion degradation of ageing structural components. *Ocean. Eng.* **2022**, *258*, 111739. [[CrossRef](#)]
5. Ding, X.; Xu, C.; Deng, M.; Zhao, Y.; Bi, X.; Hu, N. Experimental investigation of the surface corrosion damage in plates based on nonlinear Lamb wave methods. *NDT E Int.* **2021**, *121*, 102466. [[CrossRef](#)]
6. Sharma, S.; Mukherjee, A. Ultrasonic guided waves for monitoring corrosion in submerged plates. *Struct. Control Health Monit.* **2015**, *22*, 19–35. [[CrossRef](#)]

7. Zhao, G.; Wang, B.; Wang, T.; Hao, W.; Luo, Y. Detection and monitoring of delamination in composite laminates using ultrasonic guided wave. *Compos. Struct.* **2019**, *225*, 111161. [[CrossRef](#)]
8. Hervin, F.; Maio, L.; Fromme, P. Guided wave scattering at a delamination in a quasi-isotropic composite laminate: Experiment and simulation. *Compos. Struct.* **2021**, *275*, 114406. [[CrossRef](#)]
9. Lan, Z.; Saito, O.; Okabe, Y. Delamination detection in CFRP laminates using a chirp guided wave mixing technique. *NDT E Int.* **2024**, *144*, 103086. [[CrossRef](#)]
10. Fan, Z.; Lowe, M.J.S. Elastic waves guided by a welded joint in a plate. *Proc. R. Soc. A Math. Phys. Eng. Sci.* **2009**, *465*, 2053–2068. [[CrossRef](#)]
11. Ray, P.; Rajagopal, P.; Srinivasan, B.; Balasubramaniam, K. Feature-guided wave-based health monitoring of bent plates using fiber Bragg gratings. *J. Intell. Mater. Syst. Struct.* **2016**, *28*, 1211–1220. [[CrossRef](#)]
12. Hughes, J.M.; Mohabuth, M.; Kotousov, A.; Ng, C.T. The fundamental ultrasonic edge wave mode: Propagation characteristics and potential for distant damage detection. *Ultrasonics* **2021**, *114*, 106369. [[CrossRef](#)] [[PubMed](#)]
13. Yu, X.; Fan, Z.; Castaings, M.; Biateau, C. Feature guided wave inspection of bond line defects between a stiffener and a composite plate. *NDT E Int.* **2017**, *89*, 44–55. [[CrossRef](#)]
14. Fan, Z.; Castaings, M.; Lowe, M.J.S.; Biateau, C.; Fromme, P. Feature-guided waves for monitoring adhesive shear modulus in bonded stiffeners. *NDT E Int.* **2013**, *54*, 96–102. [[CrossRef](#)]
15. Ramdhas, A.; Pattanayak, R.K.; Balasubramaniam, K.; Rajagopal, P. Symmetric low-frequency feature-guided ultrasonic waves in thin plates with transverse bends. *Ultrasonics* **2015**, *56*, 232–242. [[CrossRef](#)]
16. Lan, Z.; Li, W.; Deng, M.; Okabe, Y. Combined harmonic generation of feature guided waves mixing in a welded joint. *Wave Motion* **2023**, *117*, 103103. [[CrossRef](#)]
17. Lawrie, J.B.; Kaplunov, J. Edge waves and resonance on elastic structures: An overview. *Math. Mech. Solids* **2011**, *17*, 4–16. [[CrossRef](#)]
18. Pichugin, A.V.; Rogerson, G.A. Extensional edge waves in pre-stressed incompressible plates. *Math. Mech. Solids* **2011**, *17*, 27–42. [[CrossRef](#)]
19. Wilde, M.V.; Golub, M.V.; Eremin, A.A. Experimental and theoretical investigation of transient edge waves excited by a piezoelectric transducer bonded to the edge of a thick elastic plate. *J. Sound Vib.* **2019**, *441*, 26–49. [[CrossRef](#)]
20. Zhu, H.; Kotousov, A.; Ng, C.T. Defects evaluation near edges of structural elements using the fundamental mode of edge waves. *J. Sound Vib.* **2023**, *557*, 117753. [[CrossRef](#)]
21. Wu, J.; Jiang, C.; Ng, C.-T.; Fang, H. Detection of edge delamination in composite laminates using edge waves. *Compos. Struct.* **2024**, *340*, 118177. [[CrossRef](#)]
22. Chu, J.Y.H.; Courtney, C.R.P. The Detection of Impact Damage to the Edges of CFRP Plates Using Extensional Ultrasonic Edge Waves. *J. Nondestruct. Eval.* **2021**, *40*, 88. [[CrossRef](#)]
23. Zhu, H.; Ng, C.T.; Kotousov, A. Fatigue crack detection in edges of thin-walled structures with corners using the fundamental mode of edge waves. *Ultrasonics* **2023**, *132*, 106995. [[CrossRef](#)] [[PubMed](#)]
24. Vien, B.S.; Rose, L.R.F.; Chiu, W.K. Experimental and Computational Studies on the Scattering of an Edge-Guided Wave by a Hidden Crack on a Racecourse Shaped Hole. *Materials* **2017**, *10*, 732. [[CrossRef](#)]
25. Morlock, M.B.; Kim, J.Y.; Jacobs, L.J.; Qu, J. Mixing of two co-directional Rayleigh surface waves in a nonlinear elastic material. *J. Acoust. Soc. Am.* **2015**, *137*, 281–292. [[CrossRef](#)]

Disclaimer/Publisher’s Note: The statements, opinions and data contained in all publications are solely those of the individual author(s) and contributor(s) and not of MDPI and/or the editor(s). MDPI and/or the editor(s) disclaim responsibility for any injury to people or property resulting from any ideas, methods, instructions or products referred to in the content.